ACADEMIA GREEN ENERGY

Research Article
Published: 24 March 2026
https://doi.org/10.20935/AcadEnergy8207

Second-life potential of end-of-life E-ferry cells for stationary BESS

Kun Qian[1], Johannes Diers[2], Hamzeh Beiranvand[2], Henrik Hagbarth Mikkelsen[3], Kasper M. Paasch[1], Thomas Ebel[1], Henrik Andersen[1,*]

Academic Editor: Aminhossein Jahanbin

Abstract

Introduction: This paper assesses the second-life potential of end-of-life (EoL) E-ferry cells for stationary battery energy storage systems (BESSs). Given the challenges associated with repurposing electric vehicle batteries, including heterogeneous aging profiles and complex cell balancing, this study explores an alternative pathway using E-ferry batteries that are replaced earlier due to their frequent usage in daily operations.

Materials and methods: Initial characterization of cells from multiple modules was carried out to evaluate capacity, energy retention, impedance, and charging behavior, including tests under C/3, C/2, and C/1 discharge and charge rates and additional screening for isolated outliers.

Results: Most cells exhibit consistent capacity and energy retention in the 70–80% state-of-health (SoH) range with closely clustered impedance, while one module contains an isolated outlier with significantly lower SoH (around 68%), and the large deviations can make bad cells easier to detect. Results further show that a lower C-rate is preferred, and the charging behavior analysis reveals that the charging power depends on the state of charge (SoC) and changes with the applied C-rate, which can be critical for realistic power scheduling.

Discussion: The generally uniform degradation observed across most cells, together with the SoC-dependent charging power and efficiency characteristics, highlights the need for targeted screening while confirming the practical feasibility of using these cells in stationary BESS applications.

Conclusions: Overall, the findings demonstrate that E-ferry cells, owing to their controlled operational history, earlier replacement, and generally uniform degradation, are strong candidates for second-life stationary BESSs. With appropriate screening and cell-matching procedures, these batteries can offer a practical and reliable pathway for repurposed energy storage.

Keywords: *electric ferry, second-life battery, stationary battery energy storage, cell characterization, electrochemical impedance spectroscopy*

Citation: Qian K, Diers J, Beiranvand H, Mikkelsen HH, Paasch KM, Ebel T, et al. Second-life potential of end-of-life E-ferry cells for stationary BESS. *Academia Green Energy* 2026;3. https://doi.org/10.20935/AcadEnergy8207

1. Introduction

The global push toward net zero emissions has resulted in a remarkable transformation in the transport sector, with electrification emerging as a key decarbonization strategy. This transition is particularly evident in road transportation. In 2023, almost 14 million new electric cars were registered, marking a 40% increase compared to 2022 [1]. The major automotive markets have experienced remarkable growth, with electric vehicles (EVs) comprising more than one-third and one-fifth of new car sales in China and the European Union, respectively [1]. In addition to electrifying road transport, electric vessels are increasingly operating in coastal waters for maritime applications. Nordic countries, known for their extensive ferry networks, are at the forefront of maritime electrification. As of March 2026, Norway operates 108 electric car ferries and passenger boats across 73 connections, out of a total of 225 connections [2].

Transportation electrification has significantly accelerated the adoption of lithium-ion batteries (LiBs). The global battery capacity in the energy sector has more than quadrupled from 2020, exceeding 2400 GWh in 2023. Electric vehicles have dominated this expansion, accounting for more than 90% of battery deployment and consuming over 750 GWh annually by 2023 [3]. However, the rapid transition to electrification has introduced a significant challenge regarding how to manage the growing volume of end-of-life (EoL) LiBs. Argue [4] showed that the average annual battery degradation rate for EVs has fallen from 2.3% in 2019 to 1.8% in 2024. According to the transportation industry, a battery is generally considered to have reached its EoL when its storage capacity falls to around 70% of its original capacity, i.e., when the state of health (SoH) reaches 70% [5], which means that the battery can last approximately

[1]Centre for Industrial Electronics, Faculty of Engineering, University of Southern Denmark, Sønderborg, Denmark.
[2]Chair of Power Electronics, Faculty of Engineering, Kiel University, Kiel, Germany.
[3]Marstal Maritime Academy, Marstal, Denmark.
*email: han@sdu.dk

17 years. Thus, only counting the EV batteries from 2023, over 750 GWh batteries will be retiring due to their inability to meet the desired performance by 2040. This significant volume of retiring batteries underscores the urgent need for sustainable EoL strategies. Furthermore, given the highly concentrated supply chain of battery materials, importing regions have a strategic incentive to promote battery reuse or recycling, reducing their dependence on external material sources [6].

Recycling is naturally one of the solutions for managing these EoL batteries, which can recover valuable materials such as lithium, cobalt, nickel, and manganese. However, current recycling processes face multiple challenges, including high operational costs, complex logistics for safe transportation, and energy-intensive material recovery procedures [7]. These factors, combined with fluctuating raw material prices [8], can result in recycling costs exceeding the value of recovered materials, making it an economically unsustainable solution without subsidies or technological advancement. For example, Lander et al. [9] showed that, in most cases, LiB recycling currently remains uneconomical. A detailed comparison of pyrometallurgical, hydrometallurgical, and direct-recycling routes is beyond the scope of this study. We rely on the comprehensive assessments already available in [7, 9] and use these general findings to motivate the need for second-life pathways. Challenges in recycling have prompted research into alternative approaches for managing EoL batteries, with second-life applications emerging as a promising area of focus. This approach focuses on repurposing EoL transport batteries (which still remain approximately 70% SoH) for stationary energy storage applications, where performance requirements differ significantly from transport uses. Battery energy storage systems (BESSs) present particularly suitable second-life opportunities due to their less demanding conditions (e.g., EV applications can result in almost 4 C peak power, while BESS operations typically run at 0.2 C to 0.3 C [10]).

1.1. Related work and motivation

Second-life battery (SLB) applications have been extensively investigated in the context of EVs, and recent review papers have laid a solid foundation for understanding the technical, economic, and environmental aspects of repurposing these batteries for stationary energy storage applications. Martinez-Laserna et al. [11] assessed the economic, technical, and environmental viability of reusing EV batteries in less-demanding grid-connected energy storage applications. The paper showed that SLBs offer a promising solution to offset the high upfront costs of LiBs with much lower market price estimates, making them a competitive alternative to new batteries. Profitability assessments suggest that SLBs would be valuable for applications such as demand charge management and time-of-use optimization. However, there are technical challenges, particularly regarding aging mechanisms, power and energy capabilities, and the limited availability of experimental data on long-term performance. From an environmental perspective, SLBs can significantly reduce carbon footprints and mitigate greenhouse gas emissions. Hossain et al. [12] emphasized that there are different sources of SLBs. For example, they can be batteries that reach the end of their first life due to capacity loss but also the batteries whose vehicles retire before reaching the end of their first life. The paper also investigated the manufacturing steps of the second-life battery energy storage systems (SLBESSs), including dismantling, testing, and reassembly. The review showed that SLBs could be used in many applications such as being integrated into renewable energy systems to mitigate intermittency, providing backup during maintenance outages, and peak shaving (storing energy during off-peak hours and releasing it during peak demand times). Even though SLBs hold great potential, the paper also emphasized the barriers to SLB implementation due to the lack of universal standards for battery types and the uncertainties regarding the market value of SLBs. Thus, for SLB businesses to thrive, SLBESS costs must remain low. Additionally, policies supporting the recycling and reuse of EV batteries should be established to enhance market growth. A similar study can be found in [13], where the battery degradation mechanism was also reviewed to provide the basis for assessing the health level of SLBs.

Building on that macro-level understanding, a growing body of research has focused on exploring the economic potential of SLBs through detailed empirical studies and advanced modeling. Deng et al. [14] investigated how to optimize the echelon use of retired batteries that still have a capacity above 60%. The left capacity, being converted to the left number of cycles, is incorporated in the optimization formulation to maximize the potential profit. Colarullo and Thakur [15] designed a tool to perform techno-economic analysis (TEA) for local energy communities, where different technical scenarios are considered combining PV with BESSs in both front-of- and behind-the-meter settings. The results showed that lowering the set up costs by utilizing SLBs is an opportunity already feasible, which will not only improve the energy and economic performances but also contribute to greater sustainability and circularity. Fallah and Fitzpatrick [16] also presented the TEA of using SLBs in different second-life grid-based applications, where the health level of the battery varies. The results showed that the performance of older batteries is expected to be better when contributing to grid services while keeping the investment value below 15% of the original battery cell price. However, depending on the applications, it is not always preferable to use SLBs. For example, the levelized cost of storage modeling and simulation in [17] showed that BESSs based on SLBs is likely more costly, and considering the uncertainties would make it even less economic.

Apart from the economic aspect, another focus is to investigate the challenges, often through detailed empirical studies. Zhou et al. [18] proposed a three-dimensional health feature vector, including the incremental capacity (IC) curve, DC resistance, and polarization resistance, which can be extracted from a partial charging curve. Based on which, they proposed a sorting algorithm that significantly improves the aging consistency of the sorted SLBs. Reschiglian et al. [19] presented a small-scale laboratory BESS that repurposes EoL Tesla battery modules. The system architecture was described in detail, focusing on the key components such as the battery management system (BMS), battery modules, and inverter. Preliminary test protocols are outlined to evaluate the reliability, efficiency, and energy storage capabilities, providing insights into its feasibility for real-world applications. Haram et al. [20] presented a comprehensive technical assessment and design framework for repurposing retired EV batteries for the solar-powered streetlight application, which includes battery removal, testing, and integration into a second-life application. It is worth noting that the average initial SoH was only

49.17%, which dropped to 44.75% and further to 29.25% after 100 and 350 days in their application, respectively.

In parallel, numerous pilot projects have successfully deployed second-life EV batteries in real-world settings, showcasing their potential for applications such as grid support, renewable energy integration, and optimal energy management. Nissan installed a 3 MW energy storage system at the Johan Cruijff Arena in the Netherlands in 2014, using a mix of second-life and new EV batteries alongside a 3 MW rooftop PV system [21]. The storage capacity is 2.8 MWh and the system provides backup power, reduces diesel generator use, and stabilizes the grid. Vattenfall launched a test facility in Hamburg in 2016 using 2600 recycled battery modules from over 100 BMW electric cars [22]. The 2.8 MWh system, with a 2 MW power rating, primarily helps stabilize the electricity grid at 50 Hz rather than storing energy for long periods. In 2019, Audi launched Germany's largest multi-use second-life battery storage unit (1.9 MWh) on the EUREF Campus in Berlin, using lithium-ion batteries from development vehicles [23]. The facility enables tests on intelligent energy management, including buffering excess renewable energy, stabilizing the grid, and supporting rapid EV charging. The PIONEER project supports Rome Fiumicino Airport's path to net-zero emissions by integrating a 30 MWp PV system with a 5 MW/10 MWh second-life battery storage system [24]. With the repurposed EV batteries, the system stores excess solar energy for evening peak demand and grid stabilization. These real-world implementations provide valuable insights into performance, economic viability, and technical challenges, helping to bridge the gap between theoretical studies and large-scale adoption.

Based on the literature review conducted above, SLB applications have been widely explored and extensively researched in the context of EVs, demonstrating their potential and feasibility for stationary energy storage. Recent pilot projects and techno-economic studies further highlight the growing opportunities for SLB in applications such as renewable-energy buffering, peak shaving, and backup power, reinforcing the relevance of extending battery life before recycling. However, research on repurposing batteries from electric ferries (E-ferries) remains limited. The reason is that maritime battery systems are deployed in far smaller numbers, and published research on second-life E-ferry batteries is essentially absent. From a cradle-to-grave perspective, EV batteries present challenges for second-life applications, such as heterogeneous degradation patterns, uncertain remaining useful life, and complex screening requirements, whereas E-ferry batteries follow far more predictable EoL pathways and may offer distinct advantages:

- Ferries and other maritime applications typically replace batteries earlier, often at around 70% to 80% SoH, to maintain the high energy capacity and power delivery required for operational reliability. This creates a steady supply of batteries in a range suitable for second-life applications.
- Maritime applications often operate under well-monitored conditions (e.g., specific charge/discharge cycles and environmental control). Most EV batteries use NMC or NCA chemistries whose charge/discharge behavior, voltage characteristics, and degradation mechanisms are well documented in the literature [25, 26]. E-ferries often use large-format NMC cells, which follow similar electrochemical principles, but the more predictable maritime duty cycles can lead to more uniform degradation compared to EV batteries. This predictability in aging behavior can result in repurposed batteries having consistent performance characteristics, which may significantly simplify the repurposing process.
- E-ferries utilize large battery packs, meaning that a single retired ferry battery system can provide a sufficient number of cells for one or more stationary BESS applications. In contrast, repurposing EV batteries for BESS applications often requires aggregating batteries from numerous vehicles, leading to increased complexity in cell matching, balancing, and system integration.

It is also worth noting that the maritime battery market is undergoing a transition from a one-size-fits-all approach to the use of chemistry-specific solutions tailored to different vessel profiles. Nickel Manganese Cobalt (NMC) cells have historically dominated (also the focus of this study) due to their high energy density, and they remain the preferred choice for weight-critical vessels such as electric catamarans, where high power-to-weight ratios are needed to overcome hydrodynamic drag and achieve planing. Lithium Iron Phosphate (LFP), however, is increasingly adopted in standard ferry operations because of its lower capital cost and superior thermal safety. Meanwhile, Lithium Titanate Oxide (LTO) is emerging for high-frequency shuttle routes. Despite its lower energy density and higher cost per kWh, LTO's extremely long cycle life (often exceeding 20,000 cycles) and ability to operate at high depth-of-discharge allow operators to install smaller, "right-size" battery packs that remain economically competitive over the vessel's lifetime. These trends are consistent with recent maritime battery decision-tree analyses identifying NMC, LFP, and LTO as chemistry-specific choices depending on power-to-energy ratio, cycle demand, and operational role [27]. These evolving chemistry choices underscore both the diversity and the growing strategic importance of maritime batteries, while also highlighting the need for research into their second-life potential, which remains largely unexplored.

1.2. Aims and structure of the paper

This paper aims to investigate the potential of E-ferry cells for SLB applications. The primary goal is to illustrate the specific advantages of E-ferry batteries as second-life candidates, particularly in light of the well-documented challenges associated with repurposing second-life EV batteries. To achieve this, we conduct a preliminary study to assess cell SoH and examine their behavior under various C-rates, which corresponds to the potential rates at which they would operate in BESS applications. Critical behaviors include capacity, energy, impedance, efficiency, as well as the OCV-SoC (open circuit voltage vs. state of charge) relationship. In addition, the consistency among different cells is an important factor. Another critical aspect of our research is to examine the charging behavior, with particular attention to the charging power limitation at a high SoC, which has significant implications for realistic energy scheduling and integration in stationary BESS applications.

The paper is structured as follows: Section 2 first introduces the E-ferry of interest and the used battery cells, and then presents the applied method to characterize those battery cells. Section 3 presents the test results. Section 4 discusses the results and possible future works. Section 5 concludes the paper.

2. Materials and methods

This section introduces the second-life battery source, i.e., the E-ferry batteries. Then, the test setup, procedures, and methods for the analysis of the battery cells are described.

2.1. E-ferry Ellen and the battery cell

The Municipality of Ærø (Aeroe) in Denmark launched the revolutionary E-ferry Ellen in August 2019, which broke the distance world record between charging times. The ferry, equipped with a 4.3 MWh battery, sails 40 km and up to seven times a day. The battery is divided into two separate rooms, each consisting of 10 strings, which then consists of 42 modules. Thus, there are a total of 840 modules. **Figure 1** shows the 42 modules from one string. Each module then has 32 battery cells, which have a Nickel Manganese Cobalt (NMC) chemistry and a capacity of 48 Ah. Further cell details can be obtained from **Table 1**.

Due to the large number of battery cells required for the ferry, the battery system consists of cells with nominal capacities of 48 Ah (originally supplied by a different manufacturer), 43 Ah, and 60 Ah. In this work, we present test results from the 48 Ah and 43 Ah cells as representative samples of the ferry's battery system. Compared to the 48 Ah cell specification, the 43 Ah cell has a nominal capacity and specific energy of 43 Ah and 160 Wh, respectively, measured at C/5 discharge rate.

Out of those strings, some batteries have reached the EoL for operation purposes, which has currently been defined at 80% SoH, considering the limited charging time between trips during the day and safety reserve.

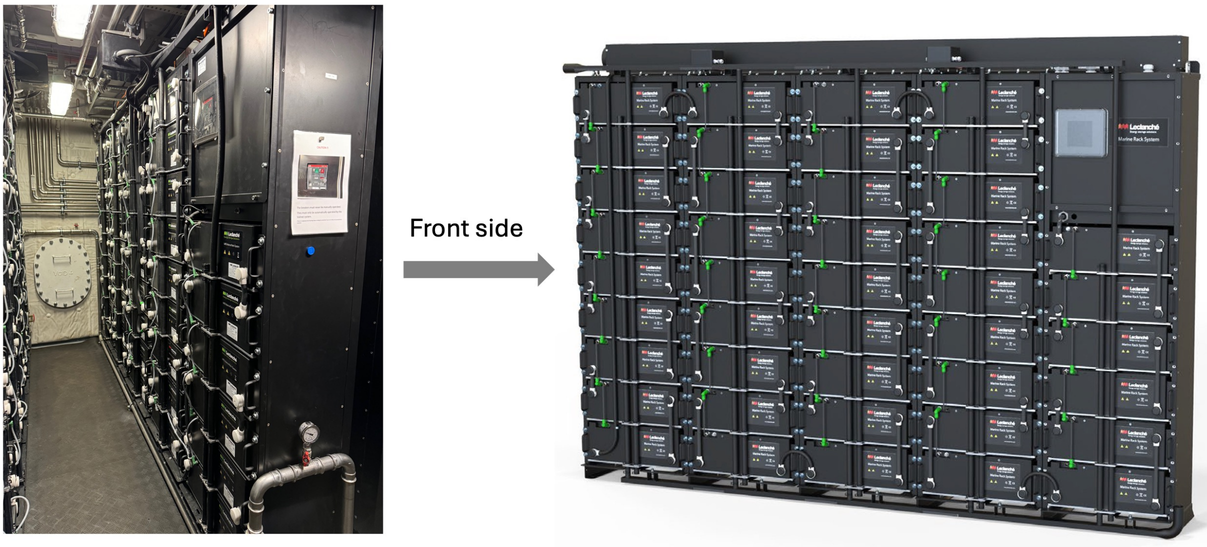

Figure 1 • Picture of one battery string, consisting of 42 modules. The front view is reproduced from [28].

Table 1 • Technical specifications of the battery cell.

Technical data	
Nominal capacity	48 Ah (measured at C/8 discharge rate, RT)
Nominal specific energy	178 Wh (measured at C/8 discharge rate, RT)
Nominal voltage	3.7 V
Voltage range	3.0 V to 4.2 V
Charge	
Charging method	CC/CV (constant voltage with limited current)
Max. charge voltage	4.2 V (+0.05 V)
Recommended charge current	48 A (1C)
Max. charge current	100 A (2C) (reduction in lifetime to be expected)
End of charge	U = 4.2 V and I < C/10
Discharge	
Recommended discharge current	48 A (1C)
Max. discharge current	144 A (3C), 20s pulse discharge 300 A (max)
End of discharge voltage	3.0 V

The batteries to be tested in this work are from four different modules. Three of them were used in the E-ferry (two from the same battery string with 48 Ah cells and one from another battery string with 43 Ah cells), and they have been taken out due to EoL. The other module is with 48 Ah cells, and it originates from the same production batch and has never been used apart from being calendar-aged in a local storage room at Ærø. We use this module as a reference since we do not have access to new batteries as the original production company went bankrupt. While it provides a stable baseline for intrinsic aging mechanisms, it cannot fully represent the cycling-induced degradation observed in the E-ferry cells. Thus, the tested battery modules are labeled with “BS16M32” (battery string 16, module 32), “BS16M33”, “BS02M18”, and “Calendar-aged” in Section 3 , respectively.

2.2. Test setup

The battery cell tests are all performed at the same ambient temperature of $20\,^{\circ}\mathrm{C}$, which is realized using the ESPEC ARL-1100 climate chamber. The cables for current injection and voltage measurement are arranged together through a cable lead-through to the inside of the chamber and are connected here with four cells using cable lugs and screws. The tests are performed by the Arbin battery tester, which measures current and voltage at the battery and is used to apply the current or voltage desired in the launched test. **Figure 2** shows the complete battery test setup, as well as the view of the battery cells inside the climate chamber.

2.3. Capacity and energy tests

For all capacity and energy tests, the cells are completely discharged in the beginning, which is performed using a constant C-rate of $-\mathrm{C}/8$. After a rest time of $30\,\mathrm{min}$, the battery is charged with a constant C-rate of C/8 and when $4.2\,\mathrm{V}$ is reached, a constant voltage is applied until a C-rate of less than C/10 is detected. For discharging, a constant C-rate of $-\mathrm{C}/8$ is applied until a battery terminal voltage of $3\,\mathrm{V}$ is reached. These rates match the capacitance test rates in the data sheet, making the experimental results comparable to the data sheet specifications. The cell charge and discharge capacity are detected according to the first charge and the subsequent discharge procedure. The coulomb counting method can be expressed as

$$Q_{\mathrm{c}} = \int_{t_{\mathrm{st}}}^{t_{\mathrm{end}}} i_{\mathrm{c}}(t)\mathrm{d}t \tag{1}$$

with the time stamps t_{st} and t_{end} representing where the charging/discharging process starts and ends, and the battery cell current is denoted by $i_{\mathrm{c}}(t)$ [29]. Q_{c} is the total charge or discharge capacity when the cell is completely charged or discharged between the time stamps. Coulomb counting is applied separately for charge and discharge without efficiency correction, since both quantities are measured directly. The coulombic efficiency (η), if desired, can then be computed as the ratio between the measured discharge and charge capacities.

Similarly, the charge and discharge energy is calculated by integrating over the charge and discharge power of the cell

$$E_{\mathrm{c}} = \int_{t_{\mathrm{st}}}^{t_{\mathrm{end}}} u_{\mathrm{c}}(t) i_{\mathrm{c}}(t)\mathrm{d}t \tag{2}$$

in which the battery terminal voltage $u_{\mathrm{c}}(t)$ is used.

2.4. Electrochemical impedance spectroscopy

The analysis of the battery cell impedance has been realized using electrochemical impedance spectroscopy (EIS). By applying an oscillating current with an RMS of $I_{\mathrm{c}} = 0.5\,\mathrm{A}$ the impedance could be detected using the parallel measured voltage of the battery. The formula

$$\underline{Z}_{\mathrm{c}}(\omega) = \frac{\underline{u}_{\mathrm{c}}(\omega)}{\underline{i}_{\mathrm{c}}(\omega)} \tag{3}$$

expresses the impedance as a function of the angular frequency [30]. Since the complex representation is used, the angular relation between voltage and current is incorporated. However, multiple frequencies must be applied to improve the overview of the battery’s electrical behavior. In the EIS tests, 20 impedance measurements have been applied per frequency decade, and the frequency range of the tests changes from $10\,\mathrm{mHz}$ to $10\,\mathrm{kHz}$. This range is commonly used for LiBs EIS because it captures the high-frequency ohmic resistance, the mid-frequency charge-transfer and interfacial processes, and the low-frequency diffusion behavior, while maintaining a practical measurement duration. The EIS is performed using the potentiostat 5000E by Gamry, which is interconnected with the Arbin battery tester that generates the current for EIS. The impedance of the current-carrying wires does not affect the test results, since a 4-wire measurement (Kelvin connection) is carried out, where the voltage is measured by two separate wires, which are attached to the battery poles right next to the current-carrying wires. Moreover, the EIS device is calibrated for the used cable length. Finally, all impedances are usually visualized in a Nyquist plot, which is a complex number plane diagram, whereas the imaginary axis is often negatively applied.

A Nyquist plot typically separates into three main regions that correspond to distinct physical processes inside the battery. The ohmic region (frequencies above approximately 1 kHz) reflects the cell’s internal resistance (R_s), measured as where the impedance transitions from inductive to capacitive behavior. The real-axis value (close to 1 kHz) in this region is commonly used as an indicator of the cell’s state of health. The mid-frequency region (roughly between 1 kHz and 0.1 Hz) captures the charge-transfer phenomena occurring at the electrode–electrolyte interfaces and within the active material. The response typically forms one or more depressed semicircles, depending on the cell chemistry and any ongoing aging processes. The shape can consist of a single arc or two partially resolved semicircles. The low-frequency region represents diffusion-controlled processes in the electrodes. This conceptual interpretation is illustrated in **Figure 3**, which presents a schematic representation of the characteristic frequency regions on a Nyquist plot. The illustration is redrawn and adapted based on the general descriptions available in prior literature (e.g., [31]).

The EIS results are further used to compare the impedance characteristics of the cells. Furthermore, the high-frequency resistance R_s is obtained from the real part of the impedance at the closest measured point to 1 kHz (1004 Hz) and later compared with the measured discharge capacities to examine whether resistance variations align with capacity variability.

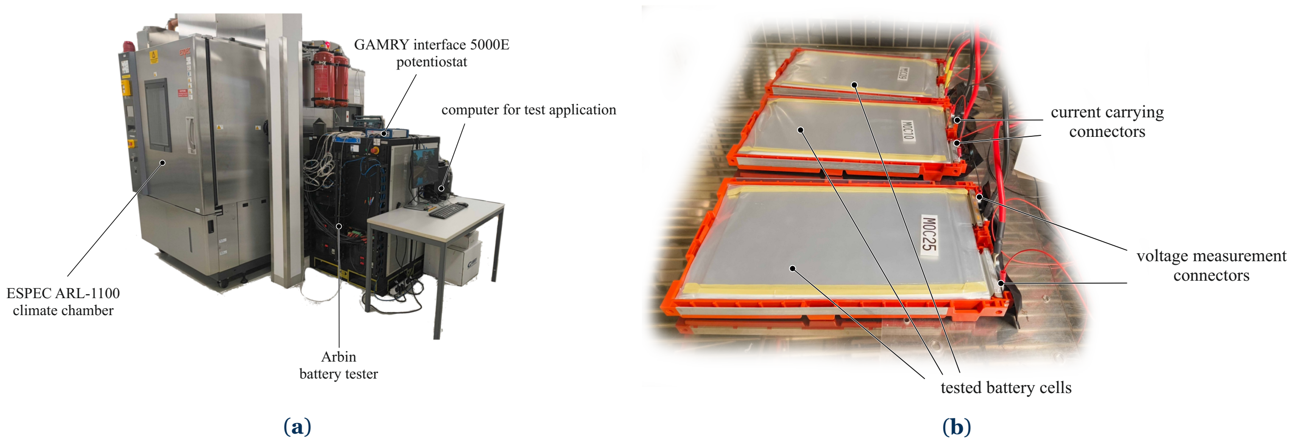

Figure 2 • Battery test setup for capacity determination and EIS. (**a**) Complete battery test setup. (**b**) Battery cells inside the climate chamber.

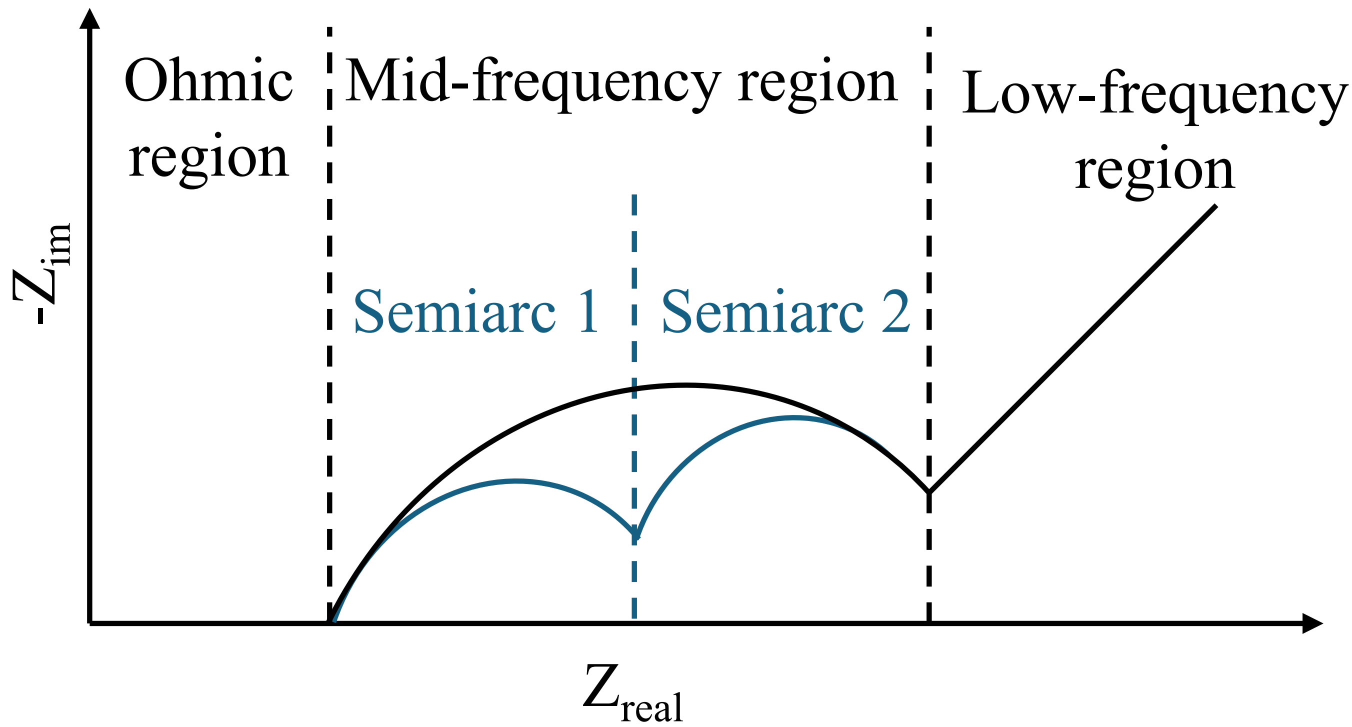

Figure 3 • Schematic representation of the typical frequency regions in a Nyquist plot. The high-frequency region corresponds to the ohmic resistance R_s, the mid-frequency region contains one or more semiarcs associated with charge-transfer and interfacial processes, and the low-frequency region reflects diffusion-dominated behavior. Reproduced from [31].

2.5. Open circuit voltage

To assess the impact of aging on SoC estimation accuracy, we compare the open circuit voltage and SoC relationship of the E-ferry cells to the calendar-aged cells, as it forms the foundation for many model-based and lookup-table-based SoC estimation methods. Two main approaches are commonly used to obtain OCV-SoC data: the incremental OCV test and a constant current (CC) test. According to the test results in [32], a low-rate CC test (e.g., C/5) can approximate the OCV-SoC curve with sufficient accuracy due to minimal polarization effects.

In this study, rather than conducting separate OCV characterization tests, we leverage the low-rate constant current cycling tests already performed for the initial capacity characterization. These tests provide a practical and efficient basis for constructing OCV-SoC curves for both calendar-aged and E-ferry cells.

Practically, since the voltage points recorded during cycling are not aligned at identical SoCs, each voltage–SoC curve is first fitted using a smooth, non-parametric interpolation. From these fitted curves, voltage values are extracted at 50 evenly spaced SoC points between 0 and 1, and the resulting values are averaged across the available cycles to obtain the OCVs. The charge and discharge curves shown later use the raw measured data, while the OCV-SoC curves are based on these interpolated and averaged values. This procedure provides a measurement-based OCV-SoC relationship without applying any parametric OCV model.

3. Results

This section presents the test results. Note that the initial analysis focused on the calendar-aged module (with 48 Ah cells) and one 48 Ah E-ferry module (BS16M32). Eight cells from each module underwent the same initial characterization procedure, after which four cells from each module were selected for high-rate cycling while the remaining cells were kept as references for potential future studies. The investigation was later expanded to include two additional modules: one 48 Ah module (BS16M33) from the same battery string as the previously tested E-ferry module, and one module (BS02M18) from a different string containing 43 Ah cells. Including these additional modules enables comparison across different operating histories and cell formats.

3.1. Initial characterization

Figure 4 shows the voltage and current curves in the initial characterization for one 43 Ah cell. The test starts with discharging at C/8, followed by a 30-minute rest. The charging process consists of the constant current (CC) phase, where the current is fixed at C/8, and the constant voltage (CV), where the voltage is fixed at the maximum charge voltage. A current value less than C/10 indicates the end of charge (as per the technical specification in **Table 1**).

The test is repeated for 8 calendar-aged cells and 24 cells that have been used in the E-ferry. **Tables 2–4** show the test results, which cover the capacity and energy during the charge and discharge phases.

The calendar-aged cells have an average capacity of 45.81 Ah (charge) and 45.79 Ah (discharge). Compared to the nominal capacity (in **Table 1**), they correspond to health levels of 95.43% and 95.40%, respectively. The variation among the cells is very small, with standard deviation (SD) values of only 0.21 Ah and relative standard deviations (RSDs) below 0.5%, indicating highly consistent behavior within the module. Similarly, the average specific energy health levels are 96.74% and 95.31% for charge and discharge, respectively, again with very low variability across the eight cells. The E-ferry cells, due to the cyclic aging during operation, exhibited much lower average health levels and larger cell-to-cell variation. For BS16M32 and BS16M33, the RSD values range from 1.19% to 1.82%, reflecting the increased heterogeneity introduced by operation. In contrast, the BS02M18 module shows a lower RSD of under 0.9%.

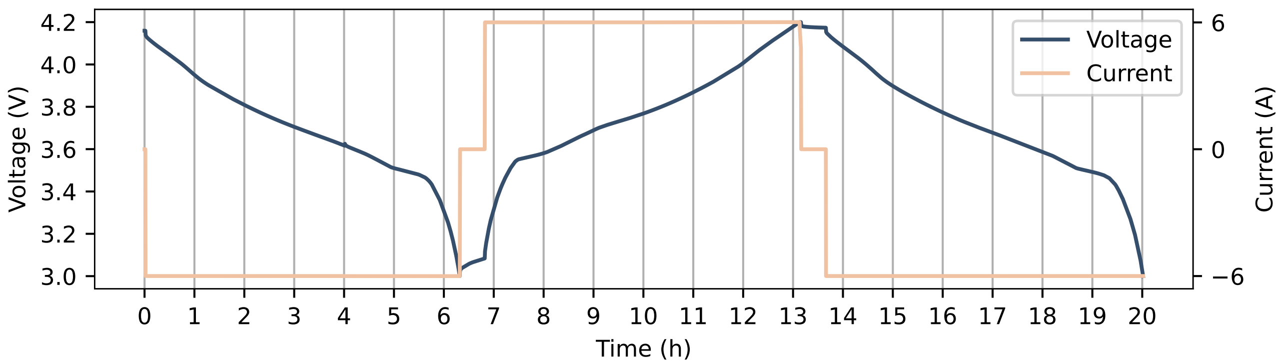

Figure 4 • Voltage and current curves for the initial characterization. The cell under test is first discharged completely, followed by charge and discharge characterization.

Table 2 • Initial characterization test result for the calendar-aged cells.

Cell No.	Capacity (Ah)		Energy (Wh)	
	Charge	**Discharge**	**Charge**	**Discharge**
1	45.60	45.65	171.30	169.23
2	45.96	46.02	172.93	170.15
3	45.56	45.49	171.28	168.71
4	45.91	45.85	172.59	169.99
5	46.01	46.04	172.81	170.65
6	45.51	45.56	171.15	168.50
7	46.11	46.02	173.34	170.63
8	45.78	45.71	172.23	169.30
Mean	45.81	45.79	172.20	169.65
SD	0.21	0.21	0.80	0.78
RSD (%)	0.46	0.45	0.46	0.46
Health (%)	95.43	95.40	96.74	95.31

Table 3 • Initial characterization test result for BS16M32 and BS16M33 cells.

Cell No.	BS16M32				BS16M33			
	Capacity (Ah)		Energy (Wh)		Capacity (Ah)		Energy (Wh)	
	Charge	Discharge	Charge	Discharge	Charge	Discharge	Charge	Discharge
1	38.03	38.15	143.78	141.21	37.70	37.88	142.54	140.25
2	38.06	38.19	143.91	141.36	37.27	37.39	140.92	138.34
3	39.01	38.90	147.58	143.89	37.82	37.93	143.00	140.43
4	38.80	38.71	146.84	143.23	37.47	37.60	141.64	139.14
5	38.12	38.21	144.13	141.49	38.44	38.38	145.53	141.93
6	38.98	38.67	147.37	143.13	38.88	38.80	147.06	143.59
7	36.80	36.94	139.17	136.83	38.45	38.40	145.50	142.05
8	38.77	38.67	146.59	143.15	38.62	38.55	146.18	142.61
Mean	38.27	38.24	144.72	141.57	38.08	38.12	144.05	141.04
SD	0.69	0.58	2.63	2.10	0.55	0.46	2.15	1.68
RSD (%)	1.81	1.51	1.82	1.48	1.45	1.21	1.49	1.19
Health (%)	79.73	79.68	81.30	79.54	79.33	79.41	80.92	79.24

Table 4 • Initial characterization test result for the BS02M18 cells.

Cell No.	Capacity (Ah)		Energy (Wh)	
	Charge	Discharge	Charge	Discharge
1	34.08	34.12	130.84	122.93
2	34.16	34.20	130.91	123.37
3	34.82	34.85	133.42	125.67
4	34.05	34.07	130.47	123.02
5	34.36	34.33	131.89	123.58
6	34.84	34.82	133.55	125.44
7 [a]	29.27	29.22	113.73	104.53
8	34.36	34.35	131.82	123.69
Mean	34.28	34.31	131.41	123.75
SD	0.31	0.30	1.14	1.04
RSD (%)	0.89	0.87	0.87	0.84
Health (%)	79.72	79.79	82.13	77.34

[a] Bad cell, excluded from average.

Comparing the discharge energy to the charge energy, i.e., the efficiency, the calendar-aged cells have an average ratio of around 98.5%, indicating a relatively high energy efficiency of the cells. The E-ferry cells have slightly lower efficiency, with an average ratio of 97.8% and 97.9% for BS16M32 and BS16M33, respectively. BS02M18 cells have a significantly lower energy efficiency, with an average ratio of only 94.2%. Note that a bad cell (cell number 7) is found in this module, whose health level for the discharge capacity is only around 67.95%, compared to the average of the other seven cells at 79.79%. This outlier is therefore excluded from the mean, SD, and RSD values reported in **Table 4**.

Since BS16M32 and BS16M33 originate from the same battery string and share the same operating history, the data from these two modules were combined to evaluate the overall consistency of the string. **Table 5** summarizes the aggregated statistics for all sixteen cells. The resulting mean values provide a representative estimate of the string-level performance, while the SD and RSD quantify the cell-to-cell variability across both modules. The combined RSD values remain between 1.37% and 1.69%, confirming a relatively uniform behavior.

Figure 5 shows the EIS test results for the calendar-aged and E-ferry cells, measured after discharging 50% of the nominal cell capacity (24 Ah discharged for the 48 Ah cells and 21.5 Ah for the

43 Ah cells), which corresponds to an SoC slightly below 50% for aged cells due to capacity loss. For each cell, the measurement at 1004 Hz is highlighted, since it often serves as a convenient proxy for the ohmic resistance. The corresponding statistics for the real part of the impedance, including minimum, maximum, mean, SD, and RSD across all cells in each module, are summarized in **Table 6**, together with a combined column for BS16M32 and BS16M33, which originate from the same battery string.

It is important to note that the 48 Ah cells in the calendar-aged module and BS16M32/3 modules are mono-cell designs, whereas the 43 Ah cells in BS02M18 are bi-cell designs containing two electrode stacks connected in parallel. This structural difference has a direct impact on the impedance response. The mono cells exhibit only one dominant interfacial process, producing a single semicircle in the mid-frequency region. In addition, the 1004 Hz measurement lies very close to the high-frequency intercept for all mono cells. In contrast, the bi cells in BS02M18 show two distinct semiarcs due to the two electrode stacks, and the 1004 Hz point falls along the descending part of the first arc rather than at the zero-crossing of the real axis.

Regarding the near 1 kHz impedance values (real part), the calendar-aged cells show a relatively wide span, which reflects the non-uniform conditions experienced during long-term storage: without periodic cycling to homogenize the cells, small differences in local temperature and resting environment accumulate into measurable impedance differences over multiple years. The BS16M32/3 modules that have aged under cycling exhibit higher mean values but much tighter clustering (lower SD and RSD). A distinctly different behavior is observed for the BS02M18 cells. The apparent ohmic resistance at the near 1 kHz is significantly higher (2.80–3.50 mΩ) than for the mono cells. In addition, cell 7 shows a noticeable rightward shift and a broader response, indicating elevated impedance and more pronounced degradation, consistent with its reduced capacity and lower health level.

Figure 6 shows the plots of the charge and discharge voltage at different SoCs for the calendar-aged and E-ferry cells. As can be seen, the overlapping of the curves in each plot indicates that the cells from the same module behave consistently.

Table 5 • Aggregated capacity and energy statistics for cells from the BS16 battery string (BS16M32 + BS16M33).

	Capacity (Ah)		**Energy (Wh)**	
	Charge	**Discharge**	**Charge**	**Discharge**
Mean	38.20	38.21	144.48	141.41
SD	0.64	0.53	2.44	1.94
RSD (%)	1.67	1.39	1.69	1.37

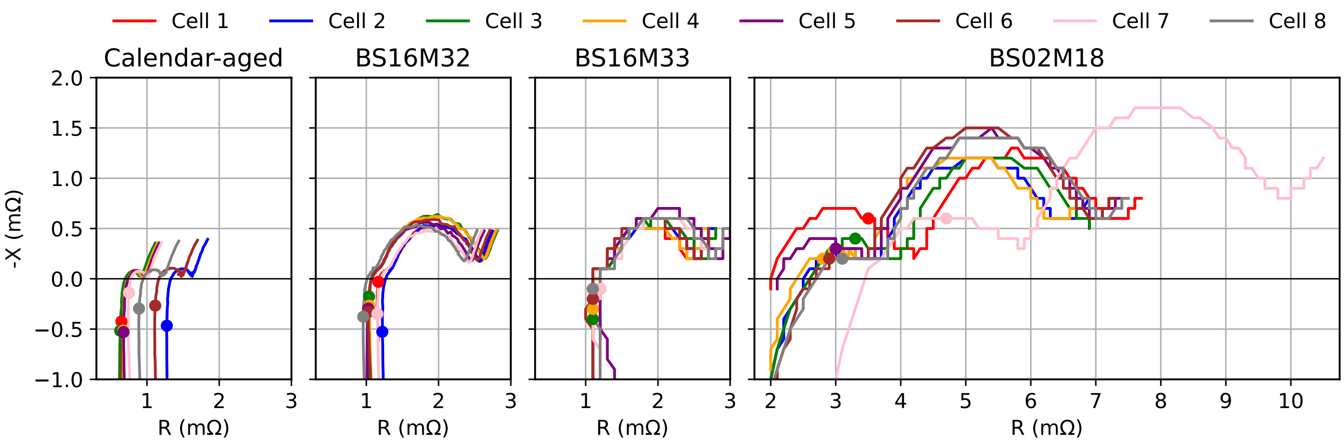

Figure 5 • Nyquist plots of the EIS measurements for the calendar-aged and E-ferry cells, recorded after discharging 50% of the nominal cell capacity. The highlighted points mark the impedance at around 1 kHz (1004 Hz), used as a practical proxy for the ohmic resistance.

Table 6 • Impedance statistics at around 1 kHz (measured at 1004 Hz) for the tested cells.

	Calendar-aged	**BS16M32**	**BS16M33**	**BS16M32/3**	**BS02M18**
Min (mΩ)	0.63	0.96	1.10	0.96	2.80
Max (mΩ)	1.27	1.22	1.20	1.22	3.50
Mean (mΩ)	0.83	1.08	1.12	1.10	3.09
SD (mΩ)	0.23	0.08	0.04	0.07	0.22
RSD (%)	27.25	7.78	3.85	6.41	7.23

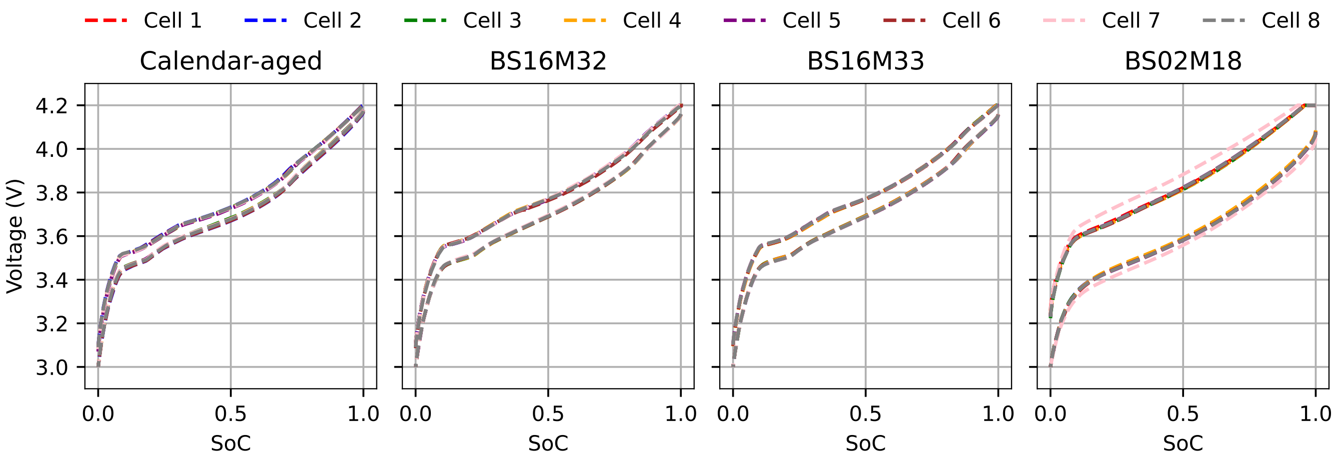

Figure 6 • Charge and discharge voltage vs. SoC at the rate C/8 (C/5 for the BS02M18 cells).

Figure 7 shows the OCV-SoC curve extracted from low-rate charge and discharge data for one cell from each module. Compared to the calendar-aged cell, the BS16M32 and BS16M33 have a higher voltage at some SoC ranges, for example, from 0.3 to 0.7. The BS02M18 cell, with a different nominal capacity rating (43 Ah), exhibits a similar OCV-SoC profile. However, noticeable deviations occur at the extremes: it shows a slightly lower voltage near full charge and a higher voltage near full discharge.

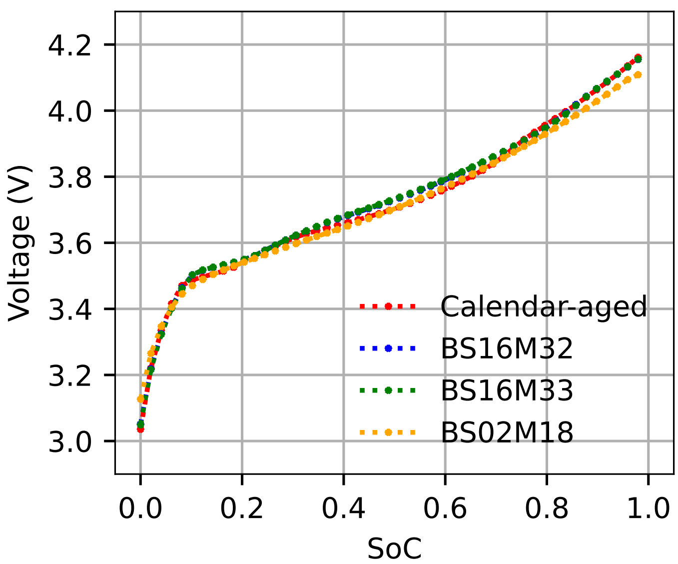

Figure 7 • Measurement-based OCV-SoC curve extracted from low-rate charge and discharge data.

Figure 8 shows the OCV-SoC curve for cells 1 and 7 from BS02M18. As can be seen, the correlation pattern between them is analogous to that between BS16M32 (or BS16M33) and calendar-aged cells, suggesting that degradation influences both battery types in a comparable manner.

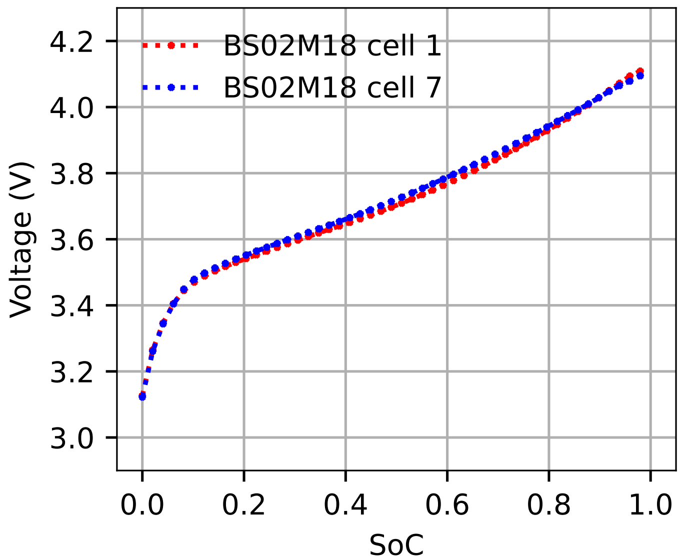

Figure 8 • Measurement-based OCV-SoC curve extracted from low-rate charge and discharge data for cells 1 and 7 from BS02M18.

Notably, the average health levels are close to 80%, which is exactly defined as the end-of-life threshold for the E-ferry application. Furthermore, the cells from the same module used in the E-ferry displayed remarkable consistency in capacity values, energy values, EIS tests, and OCV-SoC relationships (apart from cell 7 from the module BS02M18). Furthermore, the consistency remains for BS16M32 and BS16M33, which come from the same battery string. This consistency indicates that the module and string management units effectively balanced the cells and modules during operation, mitigating imbalances and ensuring uniform degradation despite extensive usage. However, testing of the module BS02M18 revealed that one of the eight cells exhibited a higher degree of degradation compared to the others, indicating that some variation can exist within the module, at least for the modules with 43 Ah cells.

3.2. Capacity and energy capability at different rates

To relate the characterization more directly to realistic second-life BESS operation, the cells were tested at three rates: C/3, C/2, and C/1. These values reflect the typical power levels reported in grid-connected stationary storage. Large BESS installations used for applications such as peak shaving or energy arbitrage commonly operate at around 0.2–0.3 C [10], while several second-life pilot projects report rated power close to C/2 (e.g., [24]). In some cases, even higher effective C-rates are observed (e.g., roughly 0.71 C in [23]). The selected rates therefore cover the relevant operational window for most stationary use cases and allow us to evaluate the expected performance and limitations of the E-ferry cells under realistic second-life loading conditions.

Figure 9 shows the voltage and current curves in the characterization at different C-rates for a calendar-aged cell. The test starts with full charging, followed by a 30-min rest. Then, discharging–rest–charging is repeated for C/3, C/2, and C/1. Note that the charging consists of CC and CV. However, the CV duration is short for the calendar-aged cell. In contrast, **Figure 10** shows the voltage and current curves under the same conditions for a BS16M32 cell, and the CV phase obviously has longer durations.

Tables 7 and **8** summarize the discharge capacity and energy capability, respectively, for 4 cells from each of the above-mentioned modules.

When cells were tested at higher C-rates (C/3, C/2 and C/1) compared to the low baseline rate (C/8 for 48 Ah cells and C/5 for 43 Ah cells), a noticeable decrease in both discharge capacity and discharge energy was observed for both calendar-aged and E-ferry cells. For the calendar-aged cells, the average reductions in discharge capacity were 0.35%, 1.27%, and 3.12% at C/3, C/2, and C/1, respectively, while for the BS16M32 cells, the corresponding reductions were 0.40%, 0.74%, and 1.76% (comparable trend for the BS16M33 cells). Similarly, discharge energy decreased by 1.00%, 2.34%, and 5.24% for the calendar-aged cells, and 1.40%, 2.40%, and 5.08% for the BS16M32 cells (again, comparable trend for the BS16M33 cells). BS02M18 cells see much higher reductions at the same rates; notably, their initial test was already performed at a higher rate of C/5 instead of C/8. The average reductions in discharge capacity were 1.87%, 4.08%, and 10.84%, and the average reductions in discharge energy were 3.35%, 6.94%, and 16.28% at C/3, C/2, and C/1, respectively.

The higher drop in the higher discharging rates is because of the increase in internal losses. At higher discharge currents, the same internal resistance leads to higher ohmic heating within the cells, reducing the effective capacity that can be delivered. Moreover, higher discharge currents also lead to higher voltage drops, which can further cause drops in discharge energy. Interestingly, the BS16M32 (and BS16M33) cells exhibited similar or even smaller relative reductions in capacity compared to the calendar-aged cells. This could be due to the operational conditioning of those cells, where regular cycling may have helped them adapt better to higher current rates by improving ion transport. However, the reductions in energy are similar, which could be due to the increased internal resistance in the BS16M32 (and BS16M33) cells, which causes higher voltage drops. Nonetheless, the consistent performance trends emphasize the impact of C-rates on usable capacity and energy.

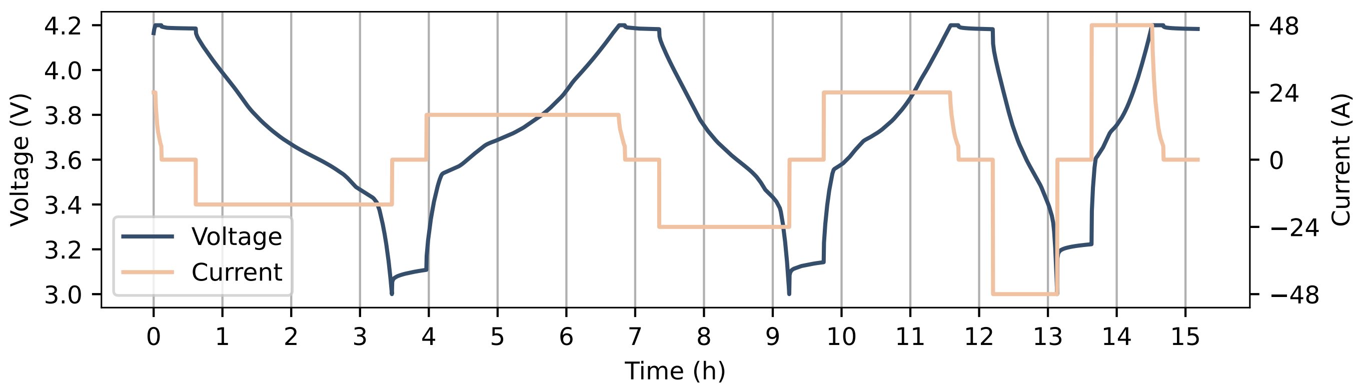

Figure 9 • Voltage and current curves for the characterization at different C-rates (C/3, C/2, and C/1) for a calendar-aged cell.

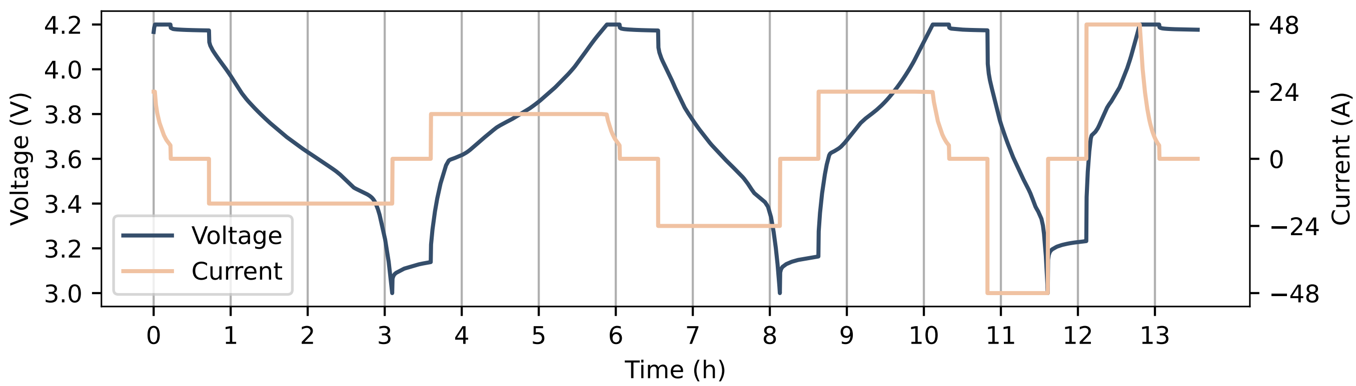

Figure 10 • Voltage and current curves for the characterization at different C-rates (C/3, C/2, and C/1) for a BS16M32 cell.

Table 7 • Discharge capacity at different C-rates.

Cell No.	Calendar-aged (Ah)			BS16M32 (Ah)			BS16M33 (Ah)			BS02M18 (Ah)		
	C/3	C/2	C/1	C/3	C/2	C/1	C/3	C/2	C/1	C/3	C/2	C/1
1	45.61	45.36	44.89	38.05	37.93	37.57	37.74	37.56	37.18	33.40	32.61	30.37
2	45.66	45.00	43.64	38.09	37.97	37.58	37.17	37.00	36.62	33.44	32.73	30.66
3	45.98	45.75	45.38	38.10	37.97	37.58	38.07	37.83	37.34	33.63	32.90	30.49
4	45.27	44.73	43.54	38.10	37.95	37.53	38.48	38.29	37.87	34.22	33.40	30.84
Average	45.63	45.21	44.36	38.09	37.96	37.57	37.87	37.67	37.25	33.67	32.91	30.59

Table 8 • Discharge energy at different C-rates.

Cell No.	Calendar-aged (Wh)			BS16M32 (Wh)			BS16M33 (Wh)			BS02M18 (Wh)		
	C/3	C/2	C/1	C/3	C/2	C/1	C/3	C/2	C/1	C/3	C/2	C/1
1	168.24	166.72	163.41	139.42	138.06	134.36	138.49	136.94	133.25	118.55	114.03	102.73
2	167.62	164.33	157.23	139.59	138.19	134.38	136.22	134.67	130.90	118.92	114.69	104.13
3	169.60	168.16	165.21	139.67	138.28	134.52	139.44	137.55	133.28	119.38	115.07	103.25
4	166.32	163.53	157.20	139.68	138.18	134.28	141.09	139.44	135.47	121.56	116.86	104.29
Average	167.95	165.69	160.76	139.59	138.18	134.38	138.81	137.15	133.22	119.60	115.16	103.60

Table 9 presents the average charge and discharge energy along with efficiency (discharge energy/charge energy) for the corresponding cells at different C-rates.

For all cell categories, the efficiency decreases as the C-rate increases. At C/3, efficiency is highest—they are 97.50%, 95.93%, and 95.99% for calendar-aged, BS16M32, and BS16M33 cells, respectively. At C/2, it drops to 96.20%, 94.45%, and 94.58%, corresponding to a relative drop of 1.33%, 1.54%, and 1.54%, respectively. Then, at C/1, it drops to 93.71%, 91.05%, and 91.24%, corresponding to a relative drop of 3.89%, 5.09%, and 4.75%, respectively. Efficiency drop at higher C-rates is expected due to increased internal resistance loss. Across the C-rates, BS16M32 and BS16M33 cells have slightly lower efficiency. Furthermore, as shown in the table, charge energy is rather consistent for the calendar-aged cells while it increases with higher C-rates for BS16M32 and BS16M33 cells. The increase suggests higher resistive losses, due to which more energy is required to push charge into the battery at higher currents. BS02M18 cells have significantly lower average efficiency at all three rates.

3.3. Quantifying the CV phase

Section 3.2 has shown that the cells used in the E-ferry have an obvious CV phase, where the cells cannot handle high currents due to the high SoC. **Table 10** summarizes the total charged energy and the charging duration, as well as those in the CV phase for different rates.

As the charging rate increases, the average CV phase duration also increases, i.e., the charging enters the CV phase relatively faster. The cell's terminal voltage rises more rapidly with higher current because the voltage drop across its internal resistance increases, along with increased polarization in the rather low C-rate range [33]. Correspondingly, the portion of energy delivered during the CV phase increases significantly, even though the total charged energy only increases slightly.

Table 9 • Charge, discharge energy, and efficiency at different C-rates.

		Calendar-aged	BS16M32	BS16M33	BS02M18
C/3	Charge (Wh)	172.25	145.51	144.61	131.05
	Discharge (Wh)	167.95	139.59	138.81	119.60
	Efficiency (%)	97.50	95.93	95.99	82.71
C/2	Charge (Wh)	172.23	146.30	145.01	129.75
	Discharge (Wh)	165.69	138.18	137.15	115.16
	Efficiency (%)	96.20	94.45	94.58	79.42
C/1	Charge (Wh)	171.55	147.59	146.01	124.21
	Discharge (Wh)	160.76	134.38	133.22	103.60
	Efficiency (%)	93.71	91.05	91.24	70.95

Table 10 • Total charged energy and charging duration, and those at the CV phase for different rates.

C rate	Cell No.	Total energy (Wh)	CV phase energy (Wh)	Energy percentage (%)	Total charge time (min)	CV phase duration (min)	Duration percentage (%)
C/3	1	145.39	6.32	4.35	147.10	10.05	6.83
	2	145.57	6.37	4.37	147.30	10.13	6.88
	3	145.57	6.23	4.28	147.28	9.95	6.76
	4	145.54	6.27	4.31	147.28	10.03	6.81
	Average	145.51	6.30	4.33	147.24	10.04	6.82
C/2	1	146.25	10.13	6.93	101.68	12.70	12.49
	2	146.37	10.19	6.96	101.82	12.78	12.56
	3	146.32	9.98	6.82	101.72	12.57	12.35
	4	146.25	10.08	6.89	101.77	12.73	12.51
	Average	146.30	10.09	6.90	101.75	12.70	12.48
C/1	1	147.67	18.60	12.60	56.77	15.12	26.63
	2	147.70	18.82	12.74	56.88	15.30	26.90
	3	147.59	18.34	12.42	56.72	15.00	26.45
	4	147.40	18.67	12.67	56.85	15.32	26.94
	Average	147.59	18.61	12.61	56.80	15.18	26.73

Figure 11 shows the average charging power at different SoCs for the 4 E-ferry cells.

The dashed lines show the nominal power calculated by multiplying the nominal voltage (3.7 V) by the respective current for each C-rate (e.g., 48 A at C/1 results in 177.6 W). Min-max shading is also applied to show the cell-to-cell variation. As demonstrated, this spread is negligible in the constant-current region due to nearly identical voltage curves (see **Figure 6**) and the same constant current, while differences appear mainly during the constant voltage phase. As shown, the measured charging power remains close to the nominal power until the cell reaches a high SoC, after which the power will drop below the nominal power. Specifically, at C/1, the expected power can only be maintained up to around 88% SoC, while for C/2 and C/3, it holds until about 93% and 96% SoC, respectively. This behavior arises because once the battery is in the CV phase, the current gradually decreases to maintain the upper voltage threshold, and consequently, the actual charging power will drop below the nominal level. Consequently, this highlights the importance of considering SoC-dependent charging power in real-world energy management and scheduling.

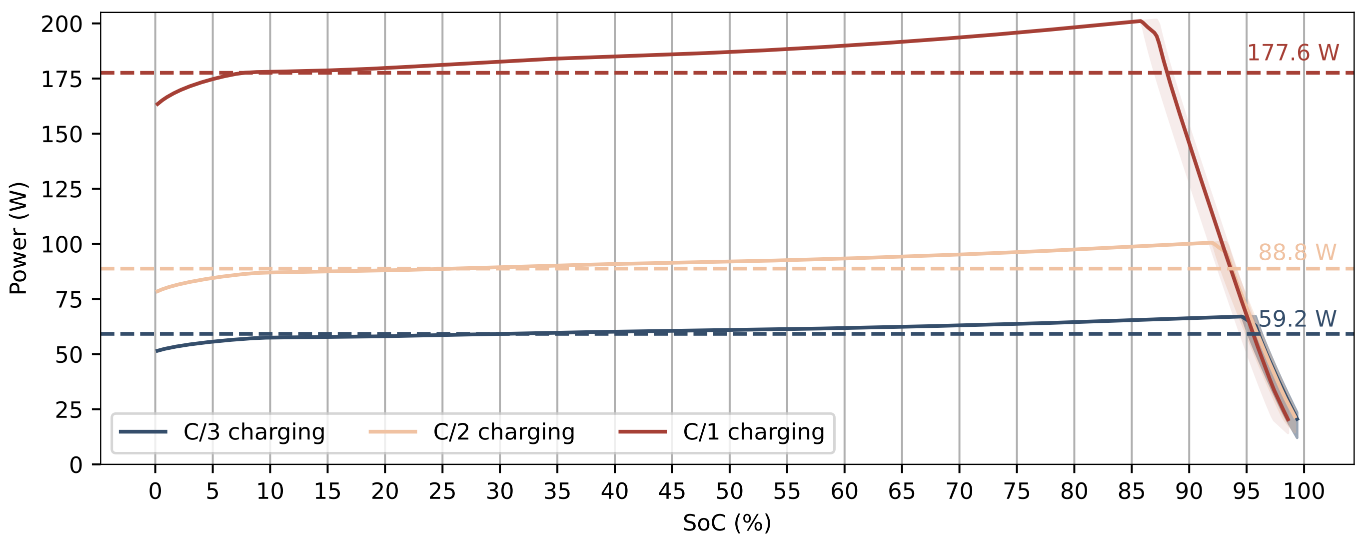

Figure 11 • Average charging power at different SoC for the 4 E-ferry cells. The dashed lines show the powers by multiplying the nominal voltage with the corresponding C-rates. Min-max shading is also applied to show the cell-to-cell variation.

4. Discussion

Before discussing the performance results in detail, it is important to highlight several practical aspects specific to E-ferry battery systems. Maritime battery deployments remain limited compared to the large and mature EV market, and the E-ferry Ellen (launched in 2019) represents one of the earliest long-range fully electric ferries. Consequently, published research on second-life E-ferry batteries is essentially absent, and repurposing studies typically rely on data from EV batteries. In Denmark, where no dedicated recycling facility exists, retired maritime battery modules must be transported to central Europe for recycling at a cost exceeding 100 Euros per module (information provided by the ferry operator). This creates a strong incentive for operators to explore second-life use as a way to extend asset value and defer costly disposal. Furthermore, availability of retired modules is not a barrier in this context, as operators prefer repurposing over paying for recycling. The performance characteristics and potential issues of the tested cells are therefore examined in the following subsections in order to evaluate their suitability for second-life applications.

4.1. On the consistency in performance across E-ferry cells

The consistency observed in the capacity health, energy health, and Electrochemical Impedance Spectroscopy (EIS) results across all eight tested BS16M32 and BS16M33 cells indicates the effectiveness of the module management unit in maintaining balance during the ferry operation. Despite extensive cycling, the cells demonstrated negligible variation in degradation patterns. Furthermore, the cells from these two modules also demonstrate a remarkable consistency, indicating the effectiveness of the battery string management.

Such consistency is crucial for second-life applications, as it opens the possibility of reusing entire modules without disassembling them into individual cells. When the cells within a module exhibit tightly clustered performance, both in capacity and impedance, the module can be repurposed as a functional unit, avoiding the labor-intensive and hazardous module disassembly. To disassemble a module, apart from the necessary equipment and machines, it would take at least two people to accomplish the job, due to the lack of standardization for the specifications and configurations of battery packs and components [34]. Based on our practical experience, the procedure typically takes 1–2 h. Additionally, the disassembly procedure is hazardous due to the potential short circuit that can happen. **Figure 12** shows the battery module after the case and electronics are disassembled, where we must be careful to avoid short circuits of the cells.

A more sustainable approach would require a task planner for robotic disassembly, such as in [35].

Furthermore, such consistency is crucial for second-life applications as it significantly reduces the need for additional screening measures such as charge–discharge tests and internal resistance measurements [34], as is also being done in this work. Unlike mixed-origin battery cells that would require such extensive screening, the E-ferry cells could potentially be seamlessly integrated into a stationary BESS with minimal work.

However, the testing of BS02M18 cells shows that some variation exists within the module. Due to the difference in the battery specification, a conclusion cannot be drawn whether variation exists in general in all modules, or only in the modules with 43 Ah bi-cells. Future studies should validate this for a larger sample set. Although seven of the BS02M18 cells exhibit relatively tight clustering, comparable to or even lower than the variability seen in the mono-cell modules, the presence of one severely degraded cell suggests that the bi-cell configuration may be more prone to producing isolated outliers. In a bi-cell, two electrode stacks operate in parallel within the same pouch, and any imbalance in current sharing, local temperature, or minor manufacturing deviation may cause one stack to age faster than the other. Such mechanisms can amplify degradation asymmetrically and lead to rare but pronounced deviations. On the other hand, the specific cell has a much lower SoH compared to others, which can potentially be identified easily to simplify the repurposing process.

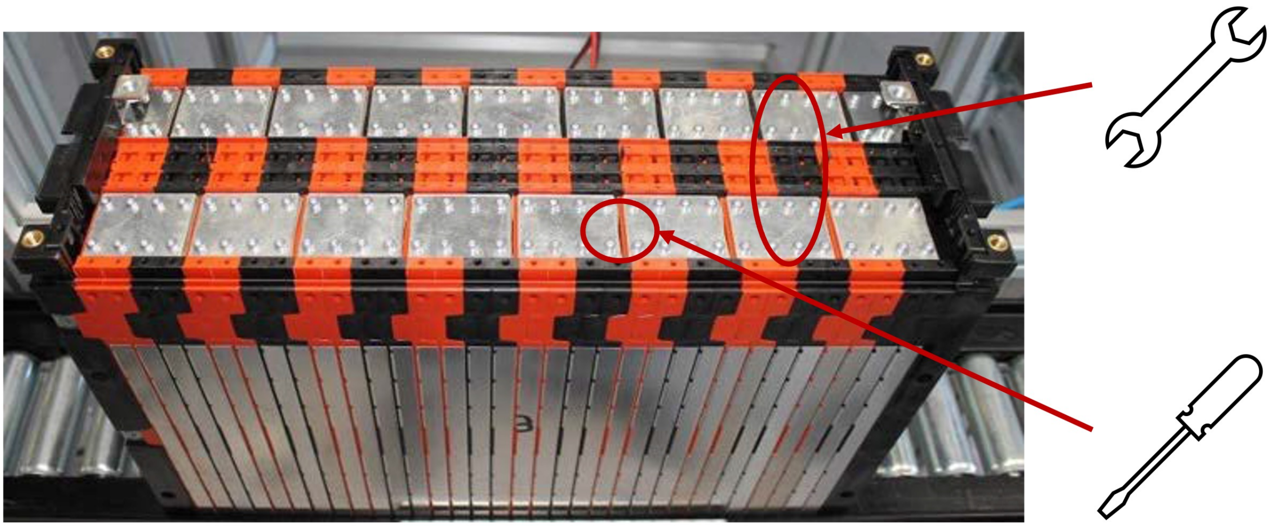

Figure 12 • Two potential short circuit situations during disassembly: (a) A metallic tool being accidentally placed on the top of two busbars, which will short two cells directly. (b) A metallic tool connecting the two busbars from the same side, which will create a path for four cells and short them.

4.2. On the efficiency trends and second-life application suitability

The E-ferry cells maintain relatively high efficiency even after extensive usage, with only a moderate decline at higher C-rates. While some efficiency losses can be attributed to increased internal ohmic resistance due to cyclic aging, the overall energy retention remains robust. Given the health state (approx. 80%), the relatively high efficiency suggests that these cells are viable for second-life applications, particularly in stationary energy storage where charge and discharge cycles operate at lower C-rates. The observed efficiency decline at higher C-rates highlights the importance of power demand considerations when using these batteries in second-life applications. For example, by increasing the C-rate from C/3 to C/2, and then to C/1 for the BS16M32 cells, the energy efficiency is 95.93%, 94.45%, and 91.05%, respectively. The efficiency drop is more significant for BS02M18 cells. To optimize second-life performance, applications should prioritize operations within moderate power ranges to minimize resistive losses. Future research includes an experimental study of further degradation of the cells and quantifying the efficiency at different SoH so that an appropriate SoH window can be determined for second-life applications.

4.3. On the CV phase and its practical implications for energy scheduling

A critical observation from the charging behavior is the SoC-dependent charging power limitation, particularly the transition into the CV phase at higher SoC levels. Traditional energy dispatch and optimization models often assume that batteries can accept power at a constant rate, neglecting the dynamic nature of charging limitations. This assumption can lead to inefficiencies in scheduling algorithms due to overestimation of charging power. This SoC-dependent maximum charging power constraint is critical for realistic scheduling, especially in applications such as grid energy storage, EV charging infrastructure, and battery-buffered renewable systems. As shown in **Figure 11**, the nominal charging power can be sustained only up to about 88% SoC at C/1, approximately 93% at C/2, and around 96% at C/3, after which the cell enters the CV region and the charging power begins to taper smoothly toward a small value (depending on the cut-off current) at full charge. The decrease appears roughly proportional to SoC, which reflects the gradual current reduction required to maintain the voltage limit. For system-level operation, this means that a BESS cannot rely on nominal charging power near the upper SoC window. Dispatch algorithms, charge rate planning, and cycle-time estimation must therefore incorporate SoC-dependent power limits to avoid overestimating charge acceptance, particularly in fast-charging or peak-shaving scenarios. On the other hand, studies often assume a limited SoC operation range to extend the battery lifetime. For example, Koubar et al. [36] limited the operational SoC range between 5% and 95%, where the nominal power would only be valid at high SoC states for the C/3 charging scenarios. Future research includes investigating whether incorporating this constraint can improve second-life battery utilization and what the optimal operational SoC range is.

5. Conclusions

In this study, we investigated the possibility of using EoL E-ferry cells for second-life stationary BESS applications. Initial results show that, in most cases, cells from the same module display a high degree of consistency in capacity, energy, and impedance, suggesting that the ferry's module management unit generally balanced degradation during operation. The same holds for the battery string management. However, further testing revealed that within certain modules, individual cells can exhibit significantly lower SoH than the rest, emphasizing the need for screening and matching processes before repurposing. Testing across various C-rates, which simulate potential operational conditions in BESS applications, revealed that the efficiency decline must be taken into account when high C-rates are used. Furthermore, the observed SoC-dependent charging power limitation underscores the need for realistic energy scheduling strategies that account for reduced power intake capability at high SoC states.

Overall, the results suggest that E-ferry cells, with their earlier replacement cycles and uniform performance, provide a robust and promising alternative for second-life energy storage solutions. The high-capacity design of the E-ferry means that fewer battery sources are required to construct a BESS based on SLBs compared to aggregating multiple EV battery packs, thereby simplifying integration and reducing system complexity. However, pre-integration testing and cell matching are essential to ensure reliable performance. Future research should focus on long-term performance assessments as well as the techno-economic assessment to demonstrate the potential of repurposed E-ferry batteries in stationary applications.

Funding

This research was sponsored by Interreg Deutschland-Danmark with funds from the SmartPowerConversion project under grant number 16-2.1-22 and by the Battery Life project (Ærø Municipality and Ærøfonden).

Author contributions

Conceptualization, K.Q. and H.A.; methodology, K.Q. and H.A.; data curation, J.D.; software, K.Q.; visualization, K.Q.; formal analysis, K.Q. and H.A.; writing—original draft, K.Q., H.A. and J.D.; writing—review and editing, J.D., H.B., H.H.M., K.M.P. and T.E.; supervision, K.M.P.; funding acquisition, H.H.M. and K.M.P. All authors have read and agreed to the published version of the manuscript.

Conflict of interest

The authors declare that they have no competing interests.

Data availability statement

The data supporting the findings of this publication can be made available upon request.

Additional information

Received: 13 November 2025

Accepted: 6 March 2026

Published: 24 March 2026

Academia Green Energy papers should be cited as *Academia Green Energy 2026*, ISSN 2998-3665, https://doi.org/10.20935/AcadEnergy8207. The journal's official abbreviation is *Acad. Energy*.

Publisher's note

Copyright

References

1. International Energy Agency (IEA). Global EV outlook 2024. 2024 [accessed on 27 December 2024]. Available from: https://www.iea.org/reports/global-ev-outlook-2024
2. Norsk Klimastiftelse. Elektriske ferger og båter. Tilnull. 2024 [accessed on 26 December 2024]. Available from: https://www.tilnull.no/energi/ferger
3. International Energy Agency (IEA). Batteries and secure energy transitions. 2024 [accessed on 27 December 2024]. Available from: https://www.iea.org/reports/batteries-and-secure-energy-transitions
4. Argue C. How long do electric car batteries last? Geotab. 2024 [accessed on 27 December 2024]. Available from: https://www.geotab.com/blog/ev-battery-health/
5. Neubauer J, Smith K, Wood E, Pesaran A. Identifying and overcoming critical barriers to widespread second use of PEV batteries. Golden (CO): National Renewable Energy Lab. (NREL); 2015. doi: 10.2172/1171780
6. Aguilar Lopez F, Lauinger D, Vuille F, Müller DB. On the potential of vehicle-to-grid and second-life batteries to provide energy and material security. Nat Commun. 2024;15(1):4179. doi: 10.1038/s41467-024-48554-0
7. Patel AN, Lander L, Ahuja J, Bulman J, Lum JKH, Pople JOD, et al. Lithium-ion battery second life: pathways, challenges and outlook. Front Chem. 2024;12:1358417. doi: 10.3389/fchem.2024.1358417
8. International Energy Agency (IEA). Price of selected battery materials and lithium-ion batteries, 2015–2024. 2024 [accessed on 20 February 2025]. Available from: https://www.iea.org/data-and-statistics/charts/price-of-selected-battery-materials-and-lithium-ion-batteries-2015-2024
9. Lander L, Cleaver T, Rajaeifar MA, Nguyen-Tien V, Elliott RJR, Heidrich O, et al. Financial viability of electric vehicle lithium-ion battery recycling. iScience. 2021;24(7):102787. doi: 10.1016/j.isci.2021.102787
10. Gao W, Cao Z, Kurdkandi NV, Fu Y, Mi, C. Evaluation of the second-life potential of the first-generation Nissan Leaf battery packs in energy storage systems. ETransportation. 2024;20:100313. doi: 10.1016/j.etran.2024.100313
11. Martinez-Laserna E, Gandiaga I, Sarasketa-Zabala E, Badeda J, Stroe DI, Swierczynski M, et al. Battery second life: hype, hope or reality? A critical review of the state of the art. Renew Sustain Energy Rev. 2018;93:701–18. doi: 10.1016/j.rser.2018.04.035
12. Hossain E, Murtaugh D, Mody J, Faruque HMR, Sunny MSH, Mohammad N. A comprehensive review on second-life batteries: current state, manufacturing considerations, applications, impacts, barriers & potential solutions, business strategies, and policies. IEEE Access. 2019;7:73215–52. doi: 10.1109/ACCESS.2019.2917859
13. Shahjalal M, Roy PK, Shams T, Fly A, Chowdhury JI, Ahmed MR, et al. A review on second-life of Li-ion batteries: prospects, challenges, and issues. Energy. 2022;241:122881. doi: 10.1016/j.energy.2021.122881
14. Deng Y, Zhang Y, Luo F, Mu Y. Operational planning of centralized charging stations utilizing second-life battery energy storage systems. IEEE Trans Sustain Energy. 2020;12(1):387–99. doi: 10.1109/TSTE.2020.3001015
15. Colarullo L, Thakur J. Second-life EV batteries for stationary storage applications in local energy communities. Renew Sustain Energy Rev. 2022;169:112913. doi: 10.1016/j.rser.2022.112913
16. Fallah N, Fitzpatrick C. How will retired electric vehicle batteries perform in grid-based second-life applications? A comparative techno-economic evaluation of used batteries in different scenarios. J Clean Prod. 2022;361:132281. doi: 10.1016/j.jclepro.2022.132281
17. Steckel T, Kendall A, Ambrose H. Applying levelized cost of storage methodology to utility-scale second-life lithium-ion battery energy storage systems. Appl Energy. 2021;300:117309. doi: 10.1016/j.apenergy.2021.117309
18. Zhou Z, Duan B, Kang Y, Shang Y, Zhang Q, Zhang C. Health feature extraction and efficient sorting of second-life lithium-ion batteries. IEEE Trans Energy Convers. 2023;39(2):1373–82. doi: 10.1109/TEC.2023.3333940
19. Reschiglian T, Sevdari K, Marinelli M. Repurposing second life EV battery for stationary energy storage applications. Proceedings of the 2024 IEEE PES Innovative Smart Grid Technologies Europe (ISGT Europe); 14–17 October 2024; Dubrovnik, Croatia. 2024. p. 1–5. doi: 10.1109/ISGTEUROPE62998.2024.10863548

20. Haram MHSM, Sarker MT, Ramasamy G, Ngu EE. Second life EV batteries: technical evaluation, design framework, and case analysis. IEEE Access. 2023;11:138799–812. doi: 10.1109/ACCESS.2023.3340044

21. PV Magazine. Nissan commissions 3 MW storage system at Amsterdam's Johan Cruijff Arena. 2018 [accessed on 20 February 2025]. Available from: https://www.pv-magazine.com/2018/06/29/nissan-commissions-3-mw-storage-system-at-johan-cruijff-arena/

22. Kihlström L-M. Brugte batterier til elbiler får nyt liv i Hamborg. Vattenfall. 2018 [accessed on 20 February 2025]. Available from: https://group.vattenfall.com/dk/nyheder-og-presse/nyheder/2016/brugte-batterier-til-elbiler-far-nyt-liv-i-hamborg

23. The Mobility House. Audi opens battery storage unit on Berlin EUREF campus. 2019 [accessed on 20 February 2025]. Available from: https://www.mobilityhouse.com/int_en/our-company/newsroom/article/audi-opens-battery-storage-unit-on-berlin-euref-campus

24. Fraunhofer ISE. PIONEER—airport sustainability second life battery storage. 2025 [accessed on 20 February 2025]. Available from: https://www.ise.fraunhofer.de/en/research-projects/pioneer.html

25. Li T, Yuan XZ, Zhang L, Song D, Shi K, Bock C. Degradation mechanisms and mitigation strategies of nickel-rich NMC-based lithium-ion batteries. Electrochem Energy Rev. 2020;3(1):43–80. doi: 10.1007/s41918-019-00053-3

26. Wittman R, Dubarry M, Ivanov S, Juba BW, Roman-Kustas J, Fresquez A, et al. Characterization of cycle-aged commercial NMC and NCA lithium-ion cells: I. temperature-dependent degradation. J Electrochem Soc. 2023;170(12):120538. doi: 10.1149/1945-7111/ad1450

27. Durgaprasad S, Coraddu A, Polinder H. An analysis of maritime battery requirements and a decision tree for optimal chemistry selection. Energy Rep. 2025;14:4851–71. doi: 10.1016/j.egyr.2025.11.086

28. Abrahamsen H. The E-ferry Ellen: a fully electric regional ferry. European Mobility Atlas 2021. 2021 [accessed on 26 December 2024]. Available from: https://eu.boell.org/sites/default/files/2021-07/The%20E-ferry%20Ellen%2C%20by%20Halfdan%20Abrahamsen%2C%20%C3%86r%C3%B8%20EnergyLab_2021-06-22.pdf

29. Movassagh K, Raihan A, Balasingam B, Pattipati K. A critical look at Coulomb counting approach for state of charge estimation in batteries. Energies. 2021;14(14):4074. doi: 10.3390/en14144074

30. Chang BY, Park SM. Electrochemical impedance spectroscopy. Annu Rev Anal Chem. 2010;3:207–29. doi: 10.1146/annurev.anchem.012809.102211

31. Iurilli P, Brivio C, Wood V. On the use of electrochemical impedance spectroscopy to characterize and model the aging phenomena of lithium-ion batteries: a critical review. J Power Sources. 2021;505:229860. doi: 10.1016/j.jpowsour.2021.229860

32. Gismero A, Stroe D-I, Schaltz E. Comparative study of state of charge estimation under different open circuit voltage test conditions for lithium-ion batteries. Proceedings of the IECON 2020 The 46th Annual Conference of the IEEE Industrial Electronics Society; 18–21 October 2020; Singapore. 2020. p. 1767–72. doi: 10.1109/IECON43393.2020.9254429

33. Liu S, Chen J, Zhang C, Jin L, Yang Q. Experimental study on lithium-ion cell characteristics at different discharge rates. J Energy Storage. 2022;45:103418. doi: 10.1016/j.est.2021.103418

34. Rallo H, Benveniste G, Gestoso I, Amante B. Economic analysis of the disassembling activities to the reuse of electric vehicles Li-ion batteries. Resour Conserv Recycl. 2020;159:104785. doi: 10.1016/j.resconrec.2020.104785

35. Choux M, Marti Bigorra E, Tyapin I. Task planner for robotic disassembly of electric vehicle battery pack. Metals. 2021;11(3):387. doi: 10.3390/met11030387

36. Koubar M, Lindberg O, Lingfors D, Huang P, Berg M, Munkhammar J. Techno-economical assessment of battery storage combined with large-scale photovoltaic power plants operating on energy and ancillary service markets. Appl Energy. 2025;382:125200. doi: 10.1016/j.apenergy.2024.125200